ACS central science

http://pubs.acs.org/journal/acscii

Research Article

Effect of Building Block Connectivity and Ion Solvation on Electrochemical Stability and Ionic Conductivity in Novel Fluoroether Electrolytes

Peiyuan Ma, Priyadarshini Mirmira, and Chibueze V. Amanchukwu*

Cite This: *ACS Cent. Sci.* 2021, 7, 1232−1244

Read Online

ACCESS | Metrics & More | Article Recommendations | Supporting Information

ABSTRACT: Novel electrolytes are required for the commercialization of batteries with high energy densities such as lithium metal batteries. Recently, fluoroether solvents have become promising electrolyte candidates because they yield appreciable ionic conductivities, high oxidative stability, and enable high Coulombic efficiencies for lithium metal cycling. However, reported fluoroether electrolytes have similar molecular structures, and the influence of ion solvation in modifying electrolyte properties has not been elucidated. In this work, we synthesize a group of fluoroether compounds with reversed building block connectivity where ether moieties are sandwiched by fluorinated end groups. These compounds can support ionic conductivities as high as 1.3 mS/cm (30 °C, 1 M salt concentration). Remarkably, we report that the oxidative stability of these electrolytes increases with decreasing fluorine content, a phenomenon not observed in other fluoroethers. Using Raman and other spectroscopic techniques, we show that lithium ion solvation is controlled by fluoroether molecular structure, and the oxidative stability correlates with the "free solvent" fraction. Finally, we show that these electrolytes can be cycled repeatedly with lithium metal and other battery chemistries. Understanding the impact of building block connectivity and ionic solvation structure on electrochemical phenomena will facilitate the development of novel electrolytes for next-generation batteries.

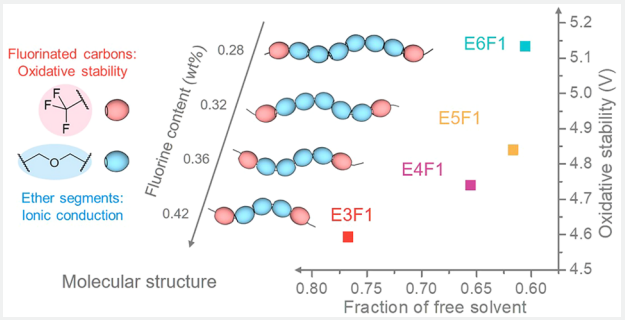

INTRODUCTION

Automotive electrification requires batteries with high energy densities. Current lithium-ion batteries have the highest energy densities commercially available but have been unable to meet the driving range and cost requirements to enable further electric vehicle market penetration.[1,2] In contrast, lithium metal batteries can have energy densities that are at least twice that of lithium-ion batteries.[3] While lithium-ion batteries use graphite as the anode, lithium metal batteries use lithium metal as the anode with a gravimetric capacity of 3860 mA h/g_{Li} compared to 372 mA h/g_c for graphite.[3,4] Furthermore, lithium has the lowest reduction potential (−3.04 V vs standard hydrogen electrode, SHE). Despite the energy density promise of lithium metal batteries, the high reactivity of lithium metal with the electrolyte[5] and uneven lithium deposition results in dendrites and electrochemically inactive lithium that limits cycle life and applicable current densities.[6]

Carbonate-based electrolytes are currently used in lithium-ion batteries because they have high ionic conductivities and can support cathodes at voltages up to 4.2 V (versus Li/Li^+, noted as V_{Li} thereafter).[7−9] However, these electrolytes are unsuitable for lithium metal batteries because they lead to Coulombic efficiencies as low as 50% and high-surface-area lithium deposits such as dendrites that can penetrate the separator.[10,11] Among the solvent classes such as carbonates, nitriles, ethers, and sulfones that have been heavily explored in lithium battery chemistries, ether (glyme) solvents have the best reductive stability.[1,9] The good reductive stability of ethers is exemplified by their use as solvents for powerful reductive agents such as $LiAlH_4$. The improved reductive stabilities lead to improved lithium metal cycling,[12,13] and ether solvents such as 1,3-dioxolane (DOL) and 1,2-dimethoxyethane (DME) can increase Coulombic efficiencies to 93.5% and 98.4%, respectively.[14,15] However, the challenges of ether solvents remain as they have very poor oxidative stability.[1,9,16] At potentials greater than 3.9−4 V_{Li}, they are oxidized significantly and cannot be used with traditional cathodes such as $LiCoO_2$.[9]

Several electrolyte engineering approaches[17] have been pursued to ameliorate the oxidative instability challenges facing ether electrolytes. Increasing the salt concentration

Received: April 26, 2021
Published: July 7, 2021

https://doi.org/10.1021/acscentsci.1c00503
ACS Cent. Sci. 2021, 7, 1232−1244

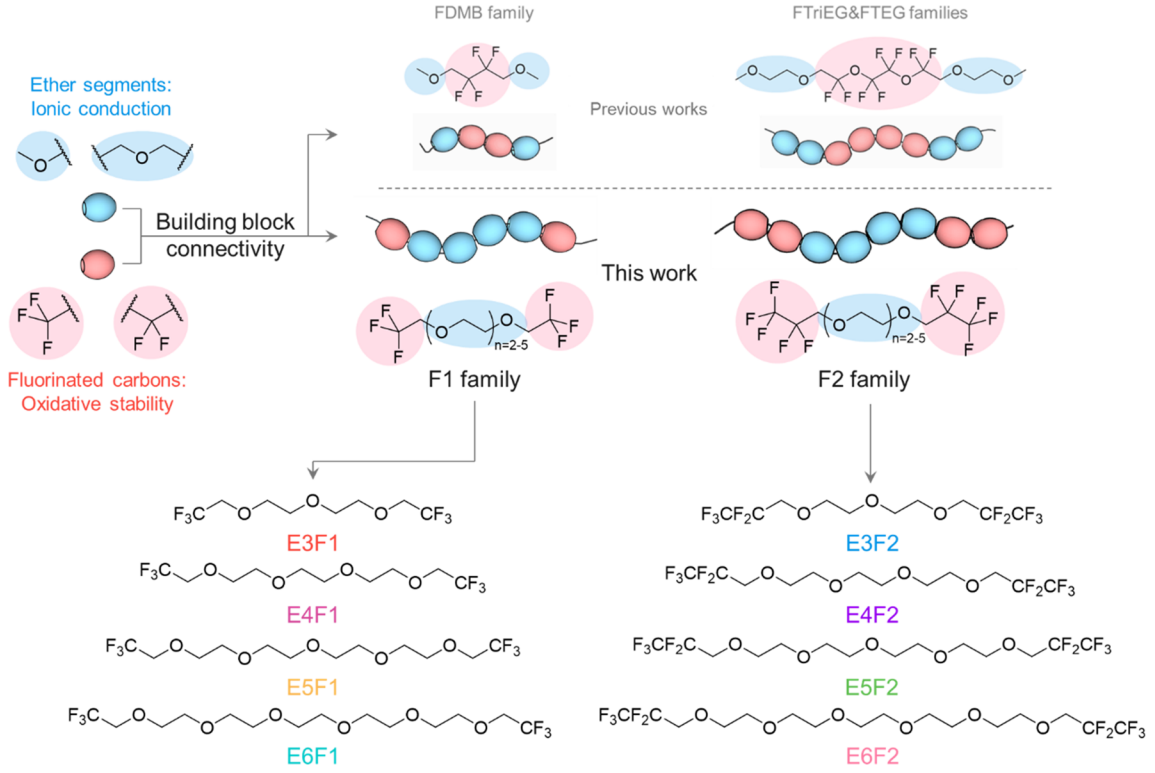

Figure 1. Molecular design. Using ether segments (blue bead) and fluorinated carbons (red bead) as building blocks, previous work has built several centrally fluorinated ethers (FDMB, FTriEG, and FTEG families).[15,26] In this work, we reverse the building block connectivity and design a group of terminal fluorinated ethers (F1 and F2 families). The fluorinated end groups and the number of ethylene oxide units are varied to explore the effects of structural factors such as fluorine content and molecular size. E3 refers to 3 ether oxygen atoms in the molecule, and F1 or F2 corresponds to the $-CF_3$ or $-CF_2CF_3$ end groups, respectively.

significantly beyond the conventional 1 M to form "high-concentration electrolytes" (HCEs) has changed the electrolyte design paradigm.[13,18,19] Increasing the salt concentration to 4 M in ethers such as DME can increase the oxidative stability from 4 to 5 V_{Li}.[20] Furthermore, HCEs can also increase the Coulombic efficiency for lithium metal deposition and stripping to as high as 98%.[21] At high salt concentrations where the molar ratio of salt to solvent is close to or above 1, solvent separated ion pairs are replaced by contact-ion pairs and aggregates where all solvent molecules participate in lithium ion solvation. The coordination between solvent and ion and the lack of free solvent molecules decreases the propensity for the solvent to be oxidized.[22] However, the increased salt concentration in these electrolytes leads to higher viscosities and, subsequently, lower ionic conductivities. Additionally, the cost of these electrolytes is much greater because lithium salt is the most expensive component.[13,22] Localized high-concentration electrolytes (LHCEs) address the challenges facing HCEs by diluting with hydrofluoroether solvents.[11,23,24] These solvents are diluents that reduce overall electrolyte viscosity and improve ion conductivity while not interrupting the ion solvation structure of contact ion pairs and aggregates present in HCEs. Since the hydrofluoroethers have high oxidative stabilities, LHCEs can also maintain a high oxidative stability.[25] Nonetheless, those diluents cannot dissolve lithium salt, and a significant fraction of inherently unstable solvents are still used.

Recently, Amanchukwu et al.[26] pursued an electrolyte chemistry approach with the molecular design of novel fluoroether electrolytes that combined the high ion conductivity and reductive stability of ethers with the oxidative stability of fluorinated compounds in a single molecule. They reported conductivities on the order of 0.1 mS/cm and oxidative stabilities as high as 5.6 V_{Li}. An improved molecular design reported by Yu et al.[15] increased the ionic conductivity to 1 mS/cm and extended oxidative stability to 6 V_{Li}. These conductive fluoroether electrolytes enabled lithium Coulombic efficiencies as high as 99.6% and the simultaneous use of high-voltage cathodes such as NMC 811 ($LiNi_{0.8}Co_{0.1}Mn_{0.1}O_2$) with cutoff potentials as high as 4.4 V_{Li}. These results have shown a pathway that emphasizes molecular design to develop novel electrolytes and overcome the challenges facing next-generation battery chemistries such as lithium metal.[27,28] However, little is known about the influence of building block connectivity. Within both works mentioned above, the same fluoroether design strategy was employed, where the fluorinated moieties are sandwiched by ether moieties (Figure 1). Although prior work by Horowitz et al.[29] illustrated a case, bis(2,2,2-trifluoroethoxy) ethane, where the building block connectivity was flipped, their study was limited to the anode/electrolyte interface whereas other physicochemical or electrochemical properties were not investigated. Furthermore, while the improvements in electrochemical stability were usually attributed to the new molecular designs of fluoroethers,[15,26] studies on HCEs have already emphasized the important role of ionic solvation structure.[22,30] We hypothesize that the influence of ionic solvation within fluoroethers could be an additional knob in modifying electrolyte properties.

In this work, we synthesize a new class of fluoroether electrolytes where the ether moiety is sandwiched between

https://doi.org/10.1021/acscentsci.1c00503
ACS Cent. Sci. 2021, 7, 1232−1244

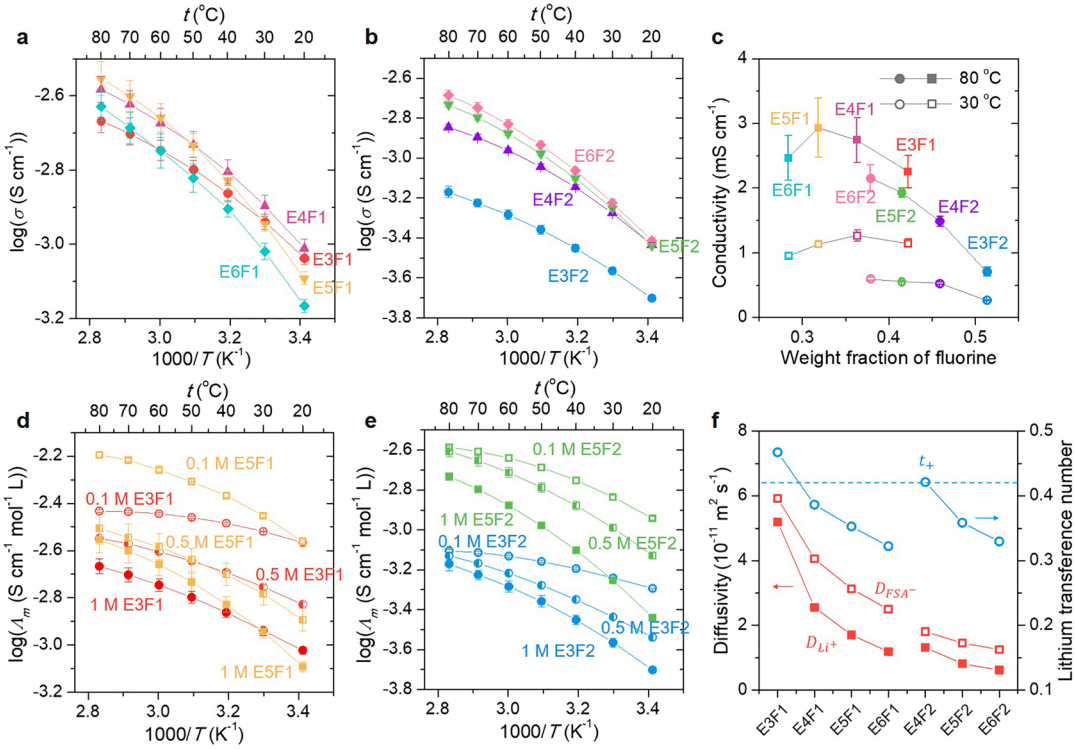

Figure 2. Ionic transport and conductivity. Ionic conductivity as a function of temperature of 1 M LiFSA dissolved in (a) F1 and (b) F2 compounds. (c) Selected ionic conductivity values at 30 and 80 °C as a function of fluorine weight fraction in both F1 and F2 compounds. Molar conductivity of LiFSA at concentrations of 0.1, 0.5, and 1 M in (d) E3F1 and E5F1 and (e) E3F2 and E5F2. (f) Ion diffusivities and lithium transference number of 1 M LiFSA dissolved in F1 and F2 compounds. The dashed horizontal line represents the lithium transference number of 1 M LiFSA in tetraglyme ($t_+ = 0.42$). All lines in this figure are to guide the eyes. The error bars in all the plots represent the standard deviation from the average of at least 3 different cells.

fluorinated functional terminal groups (Figure 1). We show that these electrolytes can maintain ionic conductivities as high as 1.3 mS/cm (30 °C) and support oxidative stabilities as high as 5.2 V_{Li}. Remarkably, as determined by linear sweep voltammetry and potentiostatic hold measurements, the new compounds show a higher oxidative stability as the fluorinated content decreases: a phenomenon not previously observed with other published fluoroethers and which contradicts intuition. Using Raman and nuclear magnetic resonance (NMR) spectroscopy, we quantify solvation effects and show that the high fluorine content of shorter molecules weakens its ability to solvate the lithium ion. Intensive ion pairing leads to a higher free solvent fraction and subsequently lower oxidative stability. Reductively, these electrolytes enable efficient lithium metal deposition and stripping with cycle lifetimes that mirror state-of-the-art glyme electrolytes. In lithium/$LiFePO_4$ (Li/LFP) cells, our electrolytes outperform commercial carbonate electrolytes. In $Li_4Ti_5O_{12}$/$LiNi_{1/3}Co_{1/3}Mn_{1/3}O_2$ (LTO/NMC 111) cells, the fluoroether electrolytes enable a significantly longer cycle life compared to conventional glymes. Hence, while oxidative stability can be increased due to the presence of fluorine in fluoroether compounds, our work shows that building block connectivity and ion solvation can play a significant role in tuning conductivity, electrochemical stability, and battery performance. Our molecular design approach for electrolyte discovery will enable a fundamental understanding of the electrolyte molecular and ionic solvation structure and will correlate electrolyte structure to electrochemical phenomena for energy-dense lithium metal batteries.

RESULTS AND DISCUSSION

Molecular Design and Synthesis. In this work, we pursue a greater understanding of the effects of building block connectivity on molecularly designed electrolytes. As shown in Figure 1, ether segments and fluorinated moieties are building blocks for the molecular design of fluorinated ether electrolytes, where the ether group enables ionic solvation and conduction while the fluorinated groups can enhance oxidative stability. Previous work on fluorinated ether electrolytes mostly focused on molecules with fluorinated moieties at the core and ether groups at the end. Amanchukwu et al.[26] reported the first class of fluorinated ether electrolytes that use a perfluorinated triethylene glycol and tetraethylene glycol units (termed FTriEG and FTEG) as the core and varying ether lengths as the end group. Follow up work by Yu et al.[15] changed the fluorinated building block to a simple perfluoroalkane and shortened the length of both fluorinated and ether blocks (termed FDMB) to simultaneously increase ionic conductivity (0.1 to 1 mS/cm) and oxidative stability (5.6 to 6 V_{Li}). In our design, the building block connectivity is reversed by using ether segments as the core and the fluorinated blocks as the end groups. We choose $-CF_3$ and $-CF_2CF_3$ as the end groups and name the resultant fluorinated ethers as F1 and F2 families, respectively, corresponding to the number of perfluorocarbons. Furthermore, the ether length is modified across both F1 and F2 families to understand the impact of molecular size and fluorine content in the molecules while retaining the same building block connectivity. The number of ether oxygens is indicated as E3−E6 with 3−6 oxygen atoms in the molecule. Hydrofluoroethers such as bis(2,2,2-

https://doi.org/10.1021/acscentsci.1c00503
ACS Cent. Sci. 2021, 7, 1232−1244

trifluoroethyl)ether (BTFE) of a similar molecular arrangement as the F1 family are commercially available and have been used as diluents in localized high-concentration electrolytes, but these compounds do not dissolve any salt or support any ionic conduction.[24,31] We will compare these new classes to previous fluorinated ether designs and conventional ether molecules that are currently of great interest in lithium metal-based batteries.

The F1 and F2 fluorinated ether molecules were synthesized using a two-step reaction starting with their corresponding glycols and fluorinated alcohols (Figure S1). The fluorinated alcohols were deprotonated using sodium hydride and reacted with bis-tosylated glycols to form the target compound (see the Experimental Section). Purification by distillation and/or flash column chromatography led to colorless or slightly yellow liquids. ^{1}H, ^{19}F, and ^{13}C nuclear magnetic resonance (NMR), Fourier transform infrared (FTIR), and gas chromatography−mass spectrometry (GC-MS) were used to confirm synthetic success and product purity (Figures S2−S4).

Ionic Conductivity and Transport. The influence of building block type (F1 vs F2) and connectivity on ionic conductivity was explored using electrochemical impedance spectroscopy (EIS). Lithium salts such as LiFSA (lithium bisfluorosulfonyl amide) can be dissolved in all of the F1 and F2 compounds at concentrations of 1 M and above. Figure 2a,b shows the ionic conductivity of 1 M LiFSA in the F1 and F2 classes as a function of temperature. All F1 compounds except for E6F1 have conductivities higher than 1 mS/cm at 30 °C, which is an order of magnitude higher than that reported for the FTriEG/FTEG compounds,[26] and similar to FDMB (3.5 mS/cm)[15] and conventional ethers such as tetraglyme (2.81 mS/cm, Figure S5). Furthermore, E3F1 can support conductivities as high as 10^{-3} mS/cm at temperatures as low as −60 °C. As shown in Figure S6, at those low temperatures, it can outperform commercial electrolytes such as 1 M $LiPF_6$ in EC/DMC (50:50 v/v) and 1 M LiFSA in tetraglyme. Despite the lower molecular weight (serving as a proxy for viscosity) of E3F1 compared to E4F1, the ionic conductivity of E3F1 is lower at room temperature. This indicates that ionic solvation in these electrolytes could play a role (discussed later). As the end group type is changed from $-CF_3$ to $-CF_2CF_3$, the F2 family shows ionic conductivities that are roughly 2 times lower than their F1 counterparts. This is due to the lower ether group fraction in the F2 family and the fact that the longer $-CF_2CF_3$ group with increased steric hindrance could inhibit lithium ion coordination. Interestingly, the conductivity trends in Figure 2b are reversed as E6F2 has the highest conductivity when compared to E5F2, E4F2, and E3F2. All F1 and F2 compounds yield ionic conductivities that are greater than 0.1 mS/cm, making them relevant as electrolytes for any nonaqueous battery chemistry. However, across both F1 and F2 compounds, the differences in room temperature ionic conductivity are not maintained at higher temperatures. For example, while the conductivity trend at room temperature is E4F1 > E3F1 > E5F1 > E6F1, the trend at 80 °C changes to E5F1 > E4F1 > E6F1 > E3F1. Again, the F2 compounds have conductivity values that coalesce at room temperature but are easily distinguishable at higher temperatures. Figure 2c shows a selection of ionic conductivity values at 30 and 80 °C as a function of fluorine weight fraction, which allows for a direct comparison of all synthesized compounds. In general, as the fluorine content decreases, the ionic conductivity increases until a certain fluorine weight fraction. At the lowest fluorine weight fractions in this work, the molecules have higher molecular weight, and viscosity increases may be responsible for the reduction in ionic conductivity. Thermally induced changes to ionic solvation structures and ion transport pathways may also be responsible for these changes and will be discussed later.

The influence of molecular structure on the activation energy barrier was further explored. The activation energy barriers for all of the molecules were extracted from the slope of the Arrhenius fit. Figure S7 shows that the activation energy barrier increases almost linearly from E3F1 (12 kJ/mol) to E5F1/E6F1 (17 kJ/mol) and from E3F2 (17 kJ/mol) to E6F2 (24 kJ/mol) as the molecular weight increases. On the other hand, the F2 compounds have higher activation energy barriers compared to their F1 counterparts (e.g., E3F2 vs E3F1), indicating that the longer fluorinated end groups add additional hindrance to ion diffusion. For electrolytes with an observed glass transition temperature (Table S2), conductivity data were also fit using the Vogel−Tammann−Fulcher (VTF) equation. Figure S8 shows that VTF equation can lead to a slightly better fitting than the Arrhenius equation, indicating that the glass transition may have an influence on lithium ion transport properties, especially in the low temperature range as shown in Figure S6.

The effect of salt concentration on ion conductivity within a select class of F1 and F2 compounds is shown in Figure 2d,e. Ionic conductivity is a function of ion concentration and mobility. When the conductivities are normalized by concentration, molar conductivity decreases as salt concentration is increased from 0.1 to 0.5 to 1 M for all electrolytes because free lithium ion activity is lowered. Even at low salt concentrations (0.1 M), E5F1 and E5F2 yield higher conductivities compared to E3F1 and E3F2, which can be explained by the lack of free charge carriers in both E3F1 and E3F2. As illustrated in the ionic solvation section later (Figure 4), LiFSA salts are not fully dissociated and mostly stay as ion pairs in E3F1 and E3F2 due to their limited number of ether oxygens.

The influence of molecular structure on ion diffusivities and the lithium transference number was studied by pulsed-field gradient nuclear magnetic resonance (PFG NMR) spectroscopy. Figure 2f shows that diffusivities of the lithium ion and FSA anion both decrease with molecular size from E3F1 to E6F1 or from E4F2 to E6F2, which could be due to increased viscosities. Lithium transference number is defined as $t_+ = D_{Li+}/(D_{Li+} + D_{FSA-})$. As shown in Figure 2f, the lithium transference number also decreases with molecular size. A lower lithium transference number means that Li^+ diffusivity is reduced relative to FSA^-, which could be explained by the ionic solvation structure as discussed later (Figure 4). In addition, 1 M LiFSA in E3F1 ($t_+ = 0.47$) has a slightly higher transference number than tetraglyme ($t_+ = 0.42$), which could compensate for its moderate ionic conductivity and improve the rate capability.

Thermal Behavior. The thermal profile of the fluorinated ether compounds and their electrolyte was studied using differential scanning calorimetry (DSC). Figure S9 shows the heating trace for all of the solvents using a heating rate of 10 °C/min from −90 to 30 °C. The F1 family and E4F2 show crystallization peaks followed by one or multiple melting peaks starting from −70 °C (E3F1) or −50 °C (longer molecules). However, for the F2 family (except E4F2), no crystallization or melting transitions were observed as the longer $-CF_2CF_3$ end

https://doi.org/10.1021/acscentsci.1c00503
ACS Cent. Sci. 2021, 7, 1232−1244

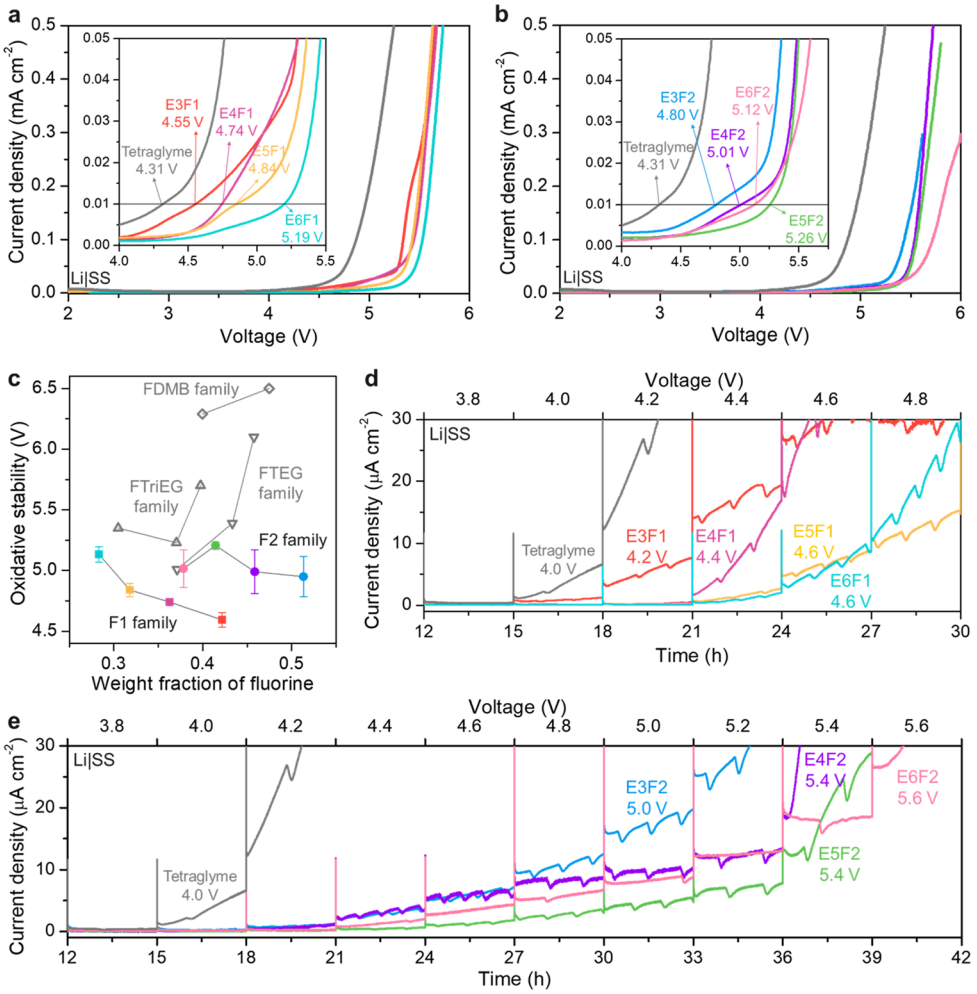

Figure 3. Oxidative stability. Linear sweep voltammetry (LSV) curve of 1 M LiFSA in (a) F1 compounds and (b) F2 compounds with tetraglyme as a control in both. Inset: zoomed-in view of the same plot with the voltage corresponding to a current density of 0.01 mA/cm^2. (c) Correlation between oxidative stability (obtained using LSV) and fluorine content in different fluorinated ether electrolytes. FTriEG/FTEG family and FDMB family data were extracted from refs 26 and 15, respectively. Color scheme of F1 and F2 family corresponds to the color scheme in parts a and b. Potentiostatic hold results of 1 M LiFSA in (d) F1 compounds and (e) F2 compounds with tetraglyme as a control in both. The cells were held at each potential for 3 h with the potential increased in 0.2 V intervals. Voltage is vs. Li/Li$^+$

groups may suppress crystallization. Glass transitions were observed for E5F1, E6F1, and E6F2 at around −80 °C, indicating that shorter compounds may also have glass transitions but are lower than the instrumental limit (−90 °C). Similarly, the FTriEG/FTEG family of compounds with different building block connectivity shows no crystallization or melting transitions, but glass transitions at temperatures around −20 °C.[26] The thermal behavior of the electrolyte mixture is distinct from the pure solvent. Figures S9−S11 show that, for both the F1 and F2 families (except for E3F1 and E3F2 at high concentrations), salt addition suppresses solvent crystallization. It provides evidence that these solvents do coordinate and solvate lithium ions, which limits the ability of the solvent to pack (crystallize). In addition, ion solvation decreases solvent mobility, which increases glass transition by about 3−4 °C from pure solvents. As shown in Figure S12, F1/F2 compounds and their electrolytes remain as supercooled liquids below their melting transition temperatures as no transition was observed in the previous cooling step. Hence, these electrolytes have a wide liquidus range up to −80 °C, which explains their ability to support low-temperature ionic conductivity that outperforms commercial electrolytes (Figure S6). However, both 1 M LiFSA E3F1 and E3F2 solutions have crystallization peaks and the E3F1 crystallization transition is shifted to −30 °C, while the 1 M LiFSA E3F2 solution crystallizes even at room temperature (Figure S13). These results indicate that ion pairing (between the lithium ion and anion) is significant in E3F1 and E3F2, and LiFSA salt has limited solubility.

Influence of Molecular Structure on Electrochemical Stability. The influence of the molecular structure and building block connectivity on oxidative stability was studied using electrochemical techniques. Linear sweep voltammetry (LSV) was performed at a scan rate of 1 mV/s in a two-electrode configuration with stainless steel or aluminum electrodes as the working electrode, lithium metal as both the reference and counter electrode, and 1 M LiFSA salt dissolved in the respective solvents as the electrolyte. An arbitrary current density value (0.01 mA/cm^2) was chosen as the threshold, and the voltage corresponding to that current density was extracted as the oxidative stability value. The promise of fluorinated ether electrolytes rests on their improved oxidative stability.[15,26] Figure 3a,b shows that the F1 and F2 families have oxidative stabilities that are higher

https://doi.org/10.1021/acscentsci.1c00503
ACS Cent. Sci. 2021, 7, 1232−1244

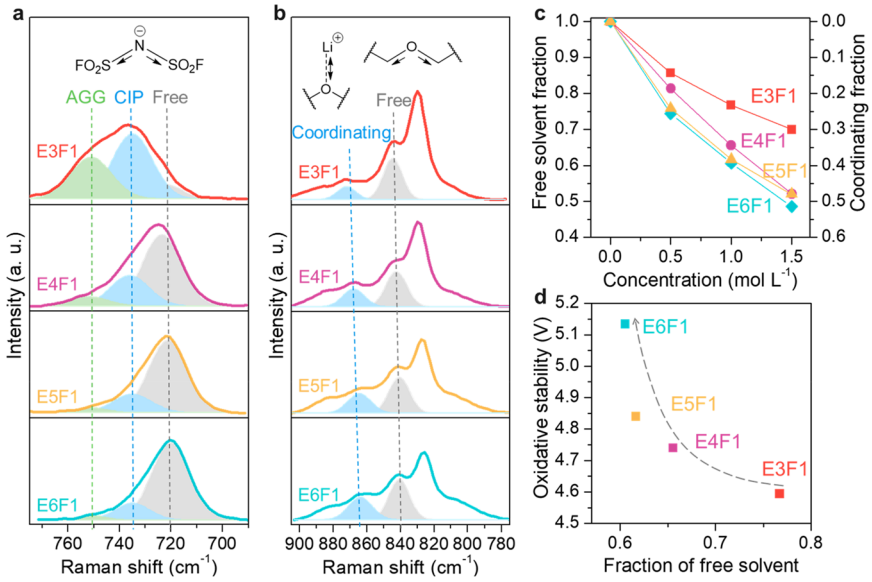

Figure 4. Solvation structure. Raman spectra of 1 M LiFSA in F1 compounds: (a) S−N−S stretching mode of FSA^-. "AGG", "CIP", and "Free" represent ion aggregates, contact-ion pairs, and free anions, respectively. (b) Raman shift range corresponding to the C−O−C stretching mode, Li^+−O breathing mode, C−F stretching mode, and C−H rocking mode of the solvent. Here, only C−O−C stretching and Li^+−O breathing peaks are highlighted in color. The "Coordinating" and "Free" peaks correspond to solvent binding to lithium ion and free solvent, respectively. (c) Fraction of free solvent and coordinating solvent for F1 compounds as a function of LiFSA salt concentration obtained from Raman spectra in parts a and b. (d) Correlation between oxidative stability (obtained using LSV) and free solvent fraction (obtained using Raman) of 1 M LiFSA in F1 electrolytes.

than those observed in conventional ethers (tetraglyme as a representative control). As expected, the extension of the end group from $-CF_3$ (F1) to $-CF_2CF_3$ (F2) leads to higher oxidative stability (Figure 3b). Surprisingly, within both the F1 and F2 classes of electrolytes, unexpected trends were observed. Figure 3a,b shows that the oxidative stability *increases* from E3F1 to E6F1 and from E3F2 to E5F2/E6F2. Figure 3c summarizes these observations and includes previously reported data on the FTriEG, FTEG, and FDMB families. In previous work, the higher the weight fraction of fluorine, the higher the oxidative stability.[15,26] Meanwhile, both F1 and F2 families contradict those trends as the oxidative stability decreases when the weight fraction of fluorine increases. These LSV traces were reproduced, and Figure S14 shows at least three LSV plots for each electrolyte composition. Figure 3c also shows that, even for the same fluorine content, building block type and connectivity play a significant role in oxidative stability: at a fluorine weight fraction ~0.42, FDMB has a greater oxidative stability compared to FTEG compared to E5F2 compared to E6F1.

The influence of electrode choice and electrochemical technique was also investigated. The stainless steel electrodes were replaced with aluminum, and Figure S15 shows that similar trends were obtained. Furthermore, potentiostatic hold experiments were performed where the cell was held at increasingly higher potentials (0.2 V intervals) for at least 3 h to monitor the rise of Faradaic currents that are due to electrolyte oxidation.[32] Figure 3d,e mirrors the LSV experiments and shows that both F1 and F2 families have higher oxidative stabilities compared to tetraglyme, with the F2 compounds greater than the F1 compounds. In addition, oxidation stability decreases with increasing fluorine content. The oxidative stability values obtained with potentiostatic holds are typically different from that reported with LSV due to the differences in technique and threshold selection. With the long-time exposures at high voltages compared to the quick scans performed with LSV, potentiostatic hold experiments are a much harsher and relevant metric for stability in most cases. However, the current density of F2 electrolytes rises slowly at the low potential range, which might be due to electrode passivation. As a result, the expected significant rise in current density is inhibited, and oxidative stabilities measured by potentiostatic holds are higher than LSV for F2 electrolytes.

Density functional theory (DFT) calculations were also performed to garner further insight into the effect of molecular structure on the redox potential. The adiabatic oxidation energy of the compounds was predicted using the procedure modified from previous work[33] (see the Experimental Section). The adiabatic oxidation energy is defined as the Gibbs free energy change of the reaction $M \rightarrow M^+ + e^-$, where the geometry of the oxidized (M^+) state is also optimized. The adiabatic oxidation energy is a measure of oxidative stability and can be converted to electrochemical potential versus Li/Li^+. To benchmark our DFT approach, we reproduced previously published adiabatic oxidation and reduction energy calculations for tetrahydrofuran, dimethyl sulfoxide, propylene carbonate, and other organic solvents (Table S3). Then, the oxidative stability of the F1 and F2 compounds was calculated and compared to the FTriEG/FTEG/FDMB families. Figure S16 shows that when the ion solvation effect is removed, the oxidative potential should decrease as the molecular length is increased or as the overall fluorine weight fraction decreases. The DFT results confirm our intuition but do not correlate with our experimental data in Figure 3c. Hence, our experimental observations cannot be explained by molecular structure alone, and ion solvation effects must be accounted for in the discussion of oxidative stability.

Influence of Molecular Structure on Ionic Solvation. The influence of salt concentration and fluorinated ether structure on ionic solvation was studied first using Raman

https://doi.org/10.1021/acscentsci.1c00503
ACS Cent. Sci. 2021, 7, 1232−1244

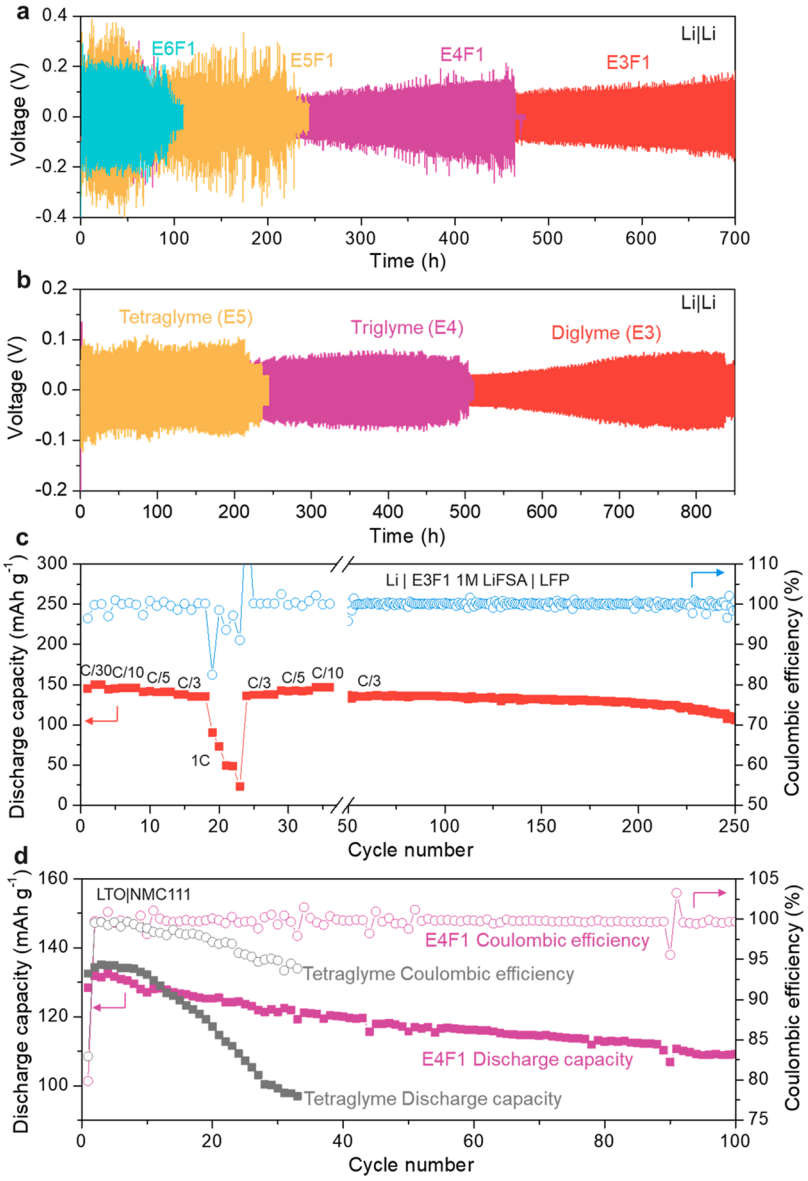

Figure 5. Battery cycling performance. Voltage versus time plot of Li/Li symmetric cells using 1 M LiFSA in (a) F1 compounds and (b) glyme solvents as electrolytes. The cells were cycled at a current density of 1 mA/cm^2 to 1 mA h/cm^2 after five formation cycles at 0.02 mA/cm^2 to 0.1 mA h/cm^2. (c) Galvanostatic cycling of the Li/LFP cell (∼1.81 mA h/cm^2 LFP loading) using 1 M LiFSA in E3F1 as the electrolyte. The cell was first cycled at rates varying from C/30 to 1C and then kept at C/3 from the 50th cycle. (d) Galvanostatic cycling of LTO/NMC 111 cells (∼1.62 mA h/cm^2 NMC loading, N/P ≈ 1.33) using 1 M LiFSA in E4F1 and tetraglyme as electrolytes at a current rate of C/5. LFP: $LiFePO_4$. LTO: $Li_4Ti_5O_{12}$. NMC 111: $LiNi_{1/3}Co_{1/3}Mn_{1/3}O_2$. Voltage is vs. Li/Li$^+$

spectroscopy. Figure 4a,b shows the anion and solvent Raman vibrations. The broad peak at around 750 cm^{-1} in Figure 4a corresponds to the S−N−S stretching mode of the FSA anion. The spectra can be deconvoluted and fitted by three components corresponding to free anions (720 cm^{-1}; Free), contact-ion pairs (734 cm^{-1}, CIP); and aggregates (751 cm^{-1}, AGG).[30] Contact-ion pairs are the most dominant in E3F1 followed by salt aggregates and a very limited fraction of free anions. In contrast, free anions are prominent in E4F1 to E6F1; however, contact-ion pairs are still present, and the fraction of contact-ion pairs decreases from E4F1 to E6F1. On the other hand, Figure 4b shows the Raman shift range corresponding to C−O−C stretching, C−F stretching, C−H rocking, and Li$^+$−O breathing. Figure S17 shows how the peaks were deconvoluted into six components. Two of these components are highlighted in Figure 4b, with the peak at 841 cm^{-1} assigned to the C−O−C stretching mode of free solvent and the peak at 867 cm^{-1} assigned to the Li$^+$−O breathing mode of the coordinating solvent.[34] As shown in Figures S18 and S19, other components such as C−H rocking and C−F stretching are barely affected by salt addition and salt concentration, indicating that they do not participate significantly in ion solvation. Hence, the fraction of free solvent can be quantified by dividing the area of the 841 cm^{-1} peak by the sum of the peak areas at 841 and 867 cm^{-1}. Figure 4c shows that the fraction of free solvent decreases as salt concentration is increased for all F1 compounds. Furthermore, E3F1 has a significantly higher fraction of free solvent (and a lower fraction of coordinating solvent) compared to other F1 compounds. Figure 4c data complements Figure 4a data that showed that ion pairing was more significant in E3F1; hence, most of the solvent is not involved in ion coordination. The

https://doi.org/10.1021/acscentsci.1c00503
ACS Cent. Sci. 2021, 7, 1232−1244

significant ion pairing can explain the lower conductivity observed in E3F1 (Figure 2a,d) despite its lower molecular weight. At higher salt concentrations where a large fraction of ions are not solvated, salt aggregates are available to crystallize as was observed in DSC data (Figure S11). Ion pair formation in E3F1 electrolyte also leads to a lithium transference number close to 0.5 (Figure 2f) because Li^+ and FSA^- are bonded in ion pairs. When the extent of ion pairing decreases from E3F1 to E6F1, more Li^+ ions are solvated by solvent molecules, and FSA^- ions are released as free anions. Since the diffusion of solvated Li^+ is retarded by the solvent, the lithium transference number is reduced from E3F1 to E6F1 as shown in Figure 2f.

The influence of ion solvation on oxidative stability was also probed. Figure 4d shows that as the fraction of free solvent decreases from E3F1 to E6F1, the oxidative stability increases. For high-concentration electrolytes and localized high-salt-concentration electrolytes, a lower free solvent fraction has been shown to lead to an increase in oxidative stability.[22,30] In those systems, the salt concentration is increased, forcing each solvent molecule to participate in ion solvation, which increases the coordinating solvent fraction. However, even when the same salt concentration is maintained for F1 compounds, there are still differences in the fraction of free solvent, and again, a lower free solvent fraction gives rise to a higher oxidative stability. Changing the salt concentration in E4F1 also allows us to vary the free solvent fraction within a single compound (Figure S20), and Figure S21 shows that the oxidative stability correlates with the free solvent fraction in the same manner. Therefore, across multiple solvents and within a specific compound (E4F1), ion solvation plays a significant role in controlling electrochemical stability. These findings show that, in addition to molecular structure, ion solvation provides a supplementary knob to tune the electrochemical phenomena of fluoroethers.

The electrolyte solvation structure was also studied using ^7Li and ^{19}F NMR spectroscopy. Figure S22a shows ^7Li NMR shifts of 1 M LiFSA dissolved in the respective F1 compounds and glyme controls. When molecular length increases from diglyme and E3F1 to tetraglyme and E6F1, an overall downfield trend is observed. Furthermore, E3F1 has an additional upfield shift of around 0.05 ppm from the other F1 electrolytes. Additionally, Figure S22b shows the ^{19}F NMR shifts of FSA anions in 1 M LiFSA solutions, where most electrolytes also shift downfield as molecular length increases. However, E3F1 contradicts this trend by resonating at a field lower than E4F1. The "unexpected" ^7Li and ^{19}F shifts of E3F1 can be explained by the dominance of ion pairing and salt aggregates: lithium ions in ion pairs and aggregates are mostly coordinated by FSA anions. Compared to the solvent, the anion can donate more electron density to Li^+ because it is negatively charged. Meanwhile, the anion loses more electron density when it is coordinating to Li^+.[35,36] Therefore, the significant ion pairing in E3F1 leads to an upfield ^7Li shift and a downfield ^{19}F shift with respect to the general trend. In summary, the distinct behavior of E3F1 in NMR data correlates to the Raman observations discussed earlier and manifests its special solvation structure dominated by ion pairing and aggregates.

Battery Performance. The influence of ion solvation and molecular structure on electrochemical cells was investigated. Lithium/lithium half cells were fabricated and cycled at 1 mA/cm^2 to 1 mA h/cm^2 after five precycling steps were done at 0.02 mA/cm^2 to 0.1 mA h/cm^2. Figure 5a shows that the E3F1 electrolyte supports the lowest overpotential for lithium deposition and stripping and enables the longest cycle life when compared to E4F1, E5F1, and E6F1. This is surprising as E3F1 is not the most conductive one in the F1 family (Figure 2a). Figure S23 shows that as the length of the fluorinated ether decreases from E6F1 to E3F1, weaker ion solvation (indicated by more ion pairing) leads to lower overpotential and longer cycle life. Recent work by Holoubek et al.[37] supports our observations as they show that ion solvation in glyme ethers can outweigh the importance of ionic conductivity in controlling the charge transfer process during lithium metal deposition and stripping. Figure 5b shows that similar trends can also be observed in Li/Li cells using conventional ethers. Figure S24 shows that E3F1 and E4F1 electrolytes outperform conventional carbonate electrolytes in Li/Li symmetric cells. In contrast, Figure S25 shows that Li/Li cells using E4F2 and E5F2 electrolytes have a poor performance at 1 mA/cm^2, which is likely due to insufficient ionic conductivity. The overall increasing overpotential from glymes to the F1 family to the F2 family can be attributed to large gaps in conductivity (~5 mS/cm for diglyme, ~1 mS/cm for F1 electrolytes, and ~0.5 mS/cm for F2 electrolytes). However, the influence of interfacial resistance should also be accounted for as discussed below.

The influence of electrolyte selection on lithium interfacial behavior was probed using EIS. Figure S26 shows the interfacial impedance of Li/Li cells during a 48 h rest period and after 6 formation cycles at 0.02 mA/cm^2 to 0.1 mA h/cm^2. The interfacial resistance decreases as a function of time for the F1 electrolytes, indicating that the fluorinated ether electrolytes passivate the lithium surface with time. Within the F1 family, E3F1 leads to the lowest interfacial resistance that is stable during the entire rest period and after cycling. In contrast, the interfacial resistance of diglyme electrolyte increases with time in the rest period and remains much higher than E3F1 after formation cycles. The interfacial resistance of E4F1 is higher during the rest period but decreases to values close to E3F1 after formation cycles. However, the E5F1 interfacial resistance is 5 times higher than that of E3F1, and the interface does not appear to stabilize. For F1 electrolytes with similar conductivities, the overpotential trend observed in Figure 5a corresponds to the interfacial resistance measured for each electrolyte.

The electrolyte performance with lithium metal was further studied in Li/Cu half cells. Figure S27 shows lithium Coulombic efficiency (CE) measurements using a modified Aurbach method as reported by Adams et al.[38] E3F1 has a higher average CE (98.9%) compared to its diglyme counterpart (95.7%). To better understand the differences in CE, Figure S28 shows scanning electron microscopy (SEM) images of residual lithium after a deposition/stripping cycle. Cells cycled in E3F1 produce compact lithium residue whereas diglyme has more dendrite-like features.

Full cells incorporating different anodes (Li and LTO) and cathodes (LFP and NMC 111) were also studied. Figure 5c shows the galvanostatic cycling of the Li/LFP cell (~1.81 mA h/cm^2 LFP loading) at current rates as high as 1C between 2.9 and 3.8 V. While Li/LFP cells can cycle repeatedly for more than 250 cycles with 1 M LiFSA in E3F1 electrolyte, the unstable charging profile of the E4F1 cell (Figure S30) shows that lithium dendrites may still form as has been reported in other systems.[39] Although both the stable interfacial resistance and high CE are indications for good lithium metal compatibility, Figure 5a,b and Figure S29 show that, compared

https://doi.org/10.1021/acscentsci.1c00503
ACS Cent. Sci. 2021, 7, 1232−1244

to E3F1, diglyme has a longer cycle life in Li/Li cells and when a low voltage cathode such as LFP is used. Recent work by Boyle et al.[40] has shown that CE alone may not be a good indicator for long-term cycling, as continuous chemical corrosion between the lithium metal and the electrolyte passivates lithium metal but leads to capacity loss. We attribute the poorer cycle life for E3F1 to continuous electrolyte consumption in long-term cycling since it should have a higher reductive potential and higher chemical reactivity with lithium as observed with other fluorinated ethers.[15,25] However, E3F1 still has an obviously improved cycling performance when compared to commercial carbonate electrolytes in either Li/Li cells (Figure 5a and Figure S24) or Li/LFP cells (Figure S29).

Since the LFP cathode operates at potentials below 4 V_{Li} and cannot showcase any improvement due to increased oxidative stability, the 4.3 V class $LiNi_{1/3}Co_{1/3}Mn_{1/3}O_2$ (NMC 111, ∼1.62 mA h/cm^2) cathode was used. Figure S31 shows that E4F1 and E5F1 electrolytes support improved capacity retention compared to E3F1 and tetraglyme in Li/NMC 111 cells, which correlates to their oxidative stability shown in Figure 3. However, noisy voltage profiles were also observed on E4F1 and E5F1, which have been attributed to dendrite growth.[39] To exclude lithium metal effects, LTO/NMC 111 cells were assembled and cycled between 1.45 and 2.75 V (corresponding to 3 to 4.3 V vs Li/Li$^+$ when the 1.55 V operating potential of LTO is accounted for).[41] Figure 5d shows that the E4F1 electrolyte supports improved cycling when compared to tetraglyme, and at least 100 cycles can be obtained at a current rate of C/5 with almost 100% Coulombic efficiency. Figure S32 shows that an even longer cycle life can be achieved by E5F1 when LTO/NMC 111 cells are cycled at a lower current rate of C/10. In addition, Figure S33 shows that E4F1 and E5F1 produce smooth voltage profiles in LTO/NMC 111 cells, which verified the effects of dendrite growth on Li/NMC 111 cells. The improved cycling performance in high-voltage full cells reflects the enhanced oxidative stability of our fluoroether compounds from conventional ethers.

CONCLUSIONS

Fluoroether electrolytes have shown great promise in high-energy-density lithium metal batteries. As fluorinated building blocks are covalently bonded with the ether moiety, fluoroethers combine high ionic conductivity, high oxidative stability, smooth lithium deposition/stripping, and high Coulombic efficiencies. However, little is understood about the effect of building block connectivity and ionic solvation on relevant electrochemical properties such as ionic conductivity, electrochemical stability, and lithium metal cycling. In this work, we synthesized a new class of fluoroether electrolytes with the ether moiety sandwiched by fluorinated segments. These electrolytes can dissolve lithium salts such as LiFSA at concentrations higher than 1 M and enable ionic conductivities at 1 mS/cm (30 °C) and above. Unlike previous work, the ionic conductivity of these compounds does not linearly correlate with ether length. Furthermore, the electrolyte oxidative stability is inversely related to the fluorine content where the higher the fluorine content, the lower the oxidative stability; an observation not seen in other fluoroethers. We show that ionic solvation within the electrolyte contributes to both observations in ionic conductivity and oxidative stability. We use Raman spectroscopy to quantify the fraction of free and coordinating solvent within the electrolyte. We show that even at conventional salt concentrations (∼1 M), the oxidative stability increases as the fraction of free solvent decreases: a phenomenon otherwise typically observed in high-concentration electrolytes. DSC and NMR measurements mirror the Raman observations and further confirm that significant ion pairing occurs in the compound with the lowest ether content (and highest fluorine fraction). Additionally, these fluoroether electrolytes were incorporated in lithium half cells, and the performances for lithium deposition and stripping mirror those observed in conventional ether solvents, despite the slightly lower ionic conductivity of fluoroethers. Finally, we fabricate lithium metal and LTO full cells with LFP and NMC 111 as the cathode to illustrate the ability of the fluoroether electrolytes to support commercially used cathodes that operate at potentials as high as 4.3 V_{Li}. Our work shows the impact building block connectivity and ion solvation in fluoroethers can have on ionic conductivity, oxidative stability, and lithium deposition/stripping.

EXPERIMENTAL SECTION

Materials. Potassium hydroxide (≥85%), sodium sulfate (anhydrous), sodium hydride (60%, in mineral oil), 2,2,3,3,3-pentafluoro-1-propanol (97%), 2,2,2-trifluoroethanol (99%), 1 M $LiPF_6$ in EC/DMC (50:50 v/v, battery grade), diethylene glycol (99%), triethylene glycol (99%), tetraethylene glycol (99%), diglyme (anhydrous), α,α,α-trifluorotoluene (99%), tetraglyme (anhydrous), and 4 Å molecular sieves were purchased from Sigma-Aldrich. Acetone (99.5%), tetrahydrofuran (certified grade, with 0.025% butylated hydroxytoluene as a preservative), dichloromethane (99.5%), hexanes (98.5%), ethyl acetate (99.5%), and methanol (99.8%) were purchased from Fisher. Lithium foil (750 μm thick), *p*-toluenesulfonyl chloride (98%), and triglyme (99%) were purchased from Alfa Aesar. Lithium perchlorate (99%), lithum bis(fluorosulfonyl) amide (99%), and pentaethylene glycol (95%) were purchased from Oakwood Chemical. Deuterated acetonitrile (≥99.8 atom % D) and deuterated chloroform (≥99.8 atom % D) were purchased from Cambridge Isotope Laboratories. All solvents used for preparing electrolytes were dried by 4 Å molecular sieves overnight inside an argon-filled glovebox (VigorTech, O_2 and H_2O < 1 ppm). LiFSA salt was vacuum-dried at 120 °C overnight in a heated glovebox antechamber before use and was not exposed to air at any time. Other chemicals were used as received.

Synthesis. *Tosylation of Glycols.* In a typical procedure, a round-bottom flask was charged with 38.13 g (0.2 mol) of tosyl chloride (TsCl) and 10.61 g (0.1 mol) of diethylene glycol. Then, 100 mL of dichloromethane (DCM) was added to dissolve all of the materials. The flask was cooled to 0 °C using an ice bath, and around 45 g (0.8 mol) of powdered potassium hydroxide (KOH) was added in small portions under stirring to maintain a low temperature. The resultant white suspension was kept under an ice bath for 3 h. The reaction was quenched by adding 100 mL of ice deionized water, which also dissolved excess KOH. The organic phase was separated and washed with 100 mL of deionized water twice. The combined aqueous phase was extracted by 50 mL of DCM. The combined organic phase was dried with anhydrous sodium sulfate (Na_2SO_4), and DCM was removed under a vacuum to yield 39 g of bis-tosylated diethylene glycol product as a white powder. The product was used directly in the next step without further purification.

Under similar procedures, bis-tosylated triethylene glycol was synthesized from triethylene glycol as a white powder; bis-

https://doi.org/10.1021/acscentsci.1c00503
ACS Cent. Sci. 2021, 7, 1232−1244

tosylated tetraethylene glycol and bis-tosylated pentaethylene glycol were obtained from tetraethylene glycol and pentaethylene glycol as colorless viscous liquids all in high (>90%) yield. NMR spectra of these products can be found in Figure S2.

Synthesis of Fluorinated Ethers. In the example of E3F1, a round-bottom flask was charged with nitrogen (Airgas, HP300), and all of the following steps were under nitrogen protection. 100 mL of dry tetrahydrofuran (THF) (dried by 4 Å molecular sieves overnight) was added together with 5.77 g of 60% sodium hydride (NaH) preserved in mineral oil (0.144 mol of NaH). The mixture was stirred to form a uniform gray suspension. Then, 9.99 mL (0.139 mol) of 2,2,2-trifluoroethanol was added dropwise to the suspension under an ice bath. When no more bubbles were released, 23.01 g (0.0555 mol) of bis-tosylated diethylene glycol dissolved in 100 mL of dry THF was added, and the mixture was heated to reflux. After refluxing overnight, the reaction mixture turned purple, and a large amount of precipitation was generated. The completion of the reaction was confirmed by thin layer chromatography (TLC).

The reaction system was cooled down to room temperature and then quenched first by a few drops of methanol and then 30 mL of deionized water, which also dissolved all of the precipitates. Then, THF was removed under vacuum, and the remaining was extracted using 30 mL of DCM three times. The combined organic phase was washed with 30 mL of deionized water twice and dried with anhydrous Na_2SO_4. After DCM was removed under vacuum, the crude product was distilled under reduced pressure to yield 11.21 g of E3F1 as a colorless liquid.

The rest of the F1 compounds and F2 compounds were synthesized in the same reaction conditions despite using different precursors and purification methods. As shown in Figure S1, all F1 compounds use 2,2,2-trifluoroethanol as a precursor while F2 compounds use 2,2,3,3,3-pentafluoro-1-propanol. Bis-tosylated diethylene glycol, bis-tosylated triethylene glycol, bis-tosylated tetraethylene glycol, and bis-tosylated pentaethylene glycol were used for the synthesis of E3F*x*, E4F*x*, E5F*x*, and E6F*x* compounds (x = 1 or 2), respectively. E3F2 was purified in the same manner with E3F1. E4F1 and E5F1 were first distilled at reduced pressure and then purified by a BUCHI Pure C-815 flash chromatography system (ethyl acetate/hexane = 0−0.5). E4F2, E5F2, E6F1, and E6F2 were directly purified by flash column (ethyl acetate/hexane = 0−0.5) because of their high boiling points. The purified products were passed through a PTFE filter (0.45 μm), transferred inside an argon-filled glovebox (VigorTech, O_2 and H_2O < 1 ppm), and dried with 4 Å molecular sieves. Their yield, boiling point, and density data are summarized in Table S1. Their NMR spectra, MS spectra, and FTIR spectra can also be found in the Supporting Information.

Physical Characterization. *Spectroscopy for Product Confirmation.* Fourier transform infrared (FTIR) spectroscopy was performed on a Shimadzu IRTracer-100 spectrometer in reflection mode using a diamond ATR crystal, with the frequency range 400−4000 cm^{-1}. Measurements were performed in the air and at ambient temperature and pressure. Samples were sealed in vials in an argon glovebox (O_2, H_2O < 1 ppm) prior to running the measurement. Roughly 20 μL of sample was used for the measurements, and a total of 15 scans were taken in absorbance mode. Acetone was used to clean the probe and ATR crystal.

Gas chromatography mass spectroscopy (GC-MS) was performed on an Agilent 7200B quadrupole time-of-flight GC/MS system. The sample was prepared by dissolving products into hexane (HPLC grade) at a 1:100 000 volume ratio and was passed through a PTFE filter (0.45 μm) prior to testing.

Nuclear magnetic resonance (NMR) spectroscopy was performed on a Bruker Ascend 9.4 T/400 MHz instrument. The NMR sample was prepared by dissolving several milligrams of product into 0.5 mL of deuterated chloroform.

Differential Scanning Calorimetry (DSC). DSC was performed with a TA Instruments Discovery 2500 differential scanning calorimeter. To prepare samples for DSC, around 10 mg of solvent or electrolyte was sealed in Tzero sample pans with hermetic lids inside an argon glovebox (O_2, H_2O < 1 ppm). DSC tests were conducted at a heating or cooling rate of 10 °C/min. The sample was first heated up to 80 °C and then looped between 80 and −90 °C twice.

Pause-Field Gradient Nuclear Magnetic Resonance (PFG NMR) Spectroscopy for Diffusivity Measurements. For the characterization of electrolytes, a capillary tube setup was used as described in refs 14 and 26. Capillary tubes and PTFE caps were obtained from New Era Enterprises. The electrolyte solution was first added into a capillary tube and sealed by a PTFE cap. Around 0.5 mL of deuterated acetonitrile was added to an NMR tube (Wilmad), and the capillary tube with sealed electrolyte was added subsequently. The NMR tube was capped and sealed by parafilm before being tested by a Bruker Ultrashield Plus 11.7 T/500 MHz instrument. The whole sample preparation process was done inside an argon-filled glovebox (O_2, H_2O < 1 ppm). Gradient strengths of up to 48 G/cm were used. Pulses of δ = 4.2 ms and Δ = 0.5−1 s were used (pulse sequence "ledgp2s"). Peak area was used for the fitting, and diffusion constants were obtained by fitting the following equation:

$$I = I_0 e^{-\gamma^2 g^2 \delta^2 D(\Delta - \frac{\delta}{3})}$$

where I = peak area as a function of gradient, γ = gyromagnetic ratio, g = gradient strength, δ = pulse duration, D = diffusion constant, and Δ = gradient pulse interval.

Nuclear Magnetic Resonance (NMR) Spectroscopy for Solvation Structure Characterization. To obtain calibrated ^{7}Li and ^{19}F chemical shifts while avoiding disturbing the solvation structure of electrolytes, the capillary tube setup described above was used. A reference solution having 0.1 M $LiClO_4$ and 0.1% (volumetric fraction) α,α,α-trifluorotoluene in deuterated acetonitrile was used as the external reference for ^{7}Li and ^{19}F chemical shifts. The electrolyte solution was first sealed in a capillary tube. Around 0.5 mL of reference solution was added to an NMR tube (Wilmad), and the capillary tube with sealed electrolyte was added subsequently. The NMR tube was capped and sealed by parafilm before testing with a Bruker Ascend 9.4 T/400 MHz instrument. The whole sample preparation process was done inside an argon-filled glovebox (O_2, H_2O < 1 ppm). The reference solution peak of ^{7}Li NMR spectra was calibrated to −2.80 ppm,[42] and the reference peak of ^{19}F NMR spectra was calibrated to −62.5 ppm.[43]

Raman Spectroscopy. A HORIBA LabRAM HR Evolution confocal Raman microscope was used for Raman spectroscopy. A 532 nm ULF laser was used as a light source. The sample was prepared by sealing electrolytes in glass chambers inside an argon-filled glovebox (O_2, H_2O < 1 ppm). The glass chamber

https://doi.org/10.1021/acscentsci.1c00503
ACS Cent. Sci. 2021, 7, 1232−1244

was assembled using glass slides (Chemglass life science) and silicone isolators purchased from Grace Bio-Laboratories.

Scanning Electron Microscopy (SEM). A Carl Zeiss Merlin field emission scanning electron microscope was used for SEM characterization. The lithium sample was prepared in Li/Cu cells where lithium was first deposited on a copper electrode at a current density of 1 mA/cm^2 for 1 h and then stripped at 1 mA/cm^2 until the cell voltage reached 1 V. Five precycles were performed prior to lithium deposition to clean the copper surface (at a current density of 0.02 mA/cm^2 between 0 and 1 V). Afterward, Li/Cu cells were opened in an argon-filled glovebox (O_2, H_2O < 1 ppm). The copper electrode with lithium residue was rinsed with 1,2-dimethoxyethane to remove lithium salt and dried under vacuum before being tested by SEM. Li/Cu coin cells were assembled in the same manner as that described in the Coulombic Efficiency (CE) Measurement in Li/Cu Half Cells section below.

Electrochemical Characterizations. *Electrochemical Impedance Spectroscopy (EIS).* Ionic conductivity measurements were performed in coin cells (CR2032) using stainless steel (SS) as electrodes. All coin cell parts were obtained from Xiamen TOB New Energy Technology. Coin cells were assembled in an argon glovebox (O_2, H_2O < 1 ppm) in the following manner: SS||30 μL of electrolyte||1 separator||30 μL of electrolyte||SS. The stainless steel electrode has a diameter of 15.6 mm. A Celgard 2325 separator (Celgard LLC.) was used for most of the electrolytes except for 1 M $LiPF_6$ in EC/DMC (50:50 v/v), where a Whatman glass fiber separator (GE Healthcare Life Science) was used for better wetting. Separators were cut into 18 mm diameter disks and washed multiple times using acetone. Then, Celgard and Whatman separators were vacuum-dried at 70 and 65 °C overnight before they were transferred into the argon glovebox without air exposure (using a BUCHI B-585 glass oven). Coin cells were tested inside an ESPEC environmental chamber (BTZ-133). The temperature was first set to 80 °C and cooled in 10 degree intervals to 20 °C (or −60 °C for low-temperature conductivity) while holding at each temperature for 1 h before the EIS measurement. A Biologic VSP-300 Potentiostat was used to measure impedance spectra between 7 MHz and 100 Hz. The obtained conductivity was calibrated by a platinum-cell conductivity probe (Vernier), and a cell constant of 13 was used to calculate realistic conductivity.

Linear Sweep Voltammetry (LSV) and Potentiostatic Hold. LSV and potentiostatic hold were performed in coin cells at 20 °C using a Biologic MPG-2 potentiostat. The configuration of Li/SS cells was SS||Li||30 μL of electrolyte||1 Celgard 2325 separator||30 μL of electrolyte||SS. When aluminum foil (Al, purchased from Fisher) was used as the working electrode, the configuration of Li/Al cells was SS||Li||30 μL of electrolyte||1 Celgard 2325 separator||30 μL of electrolyte||Al||SS. The lithium electrode has a thickness of 750 μm and a diameter of 12 mm, and the surface was scratched using a toothbrush to reveal a shiny surface (this process was done for all lithium metal containing cells). The aluminum electrode has a diameter of 15 mm. All of the coin cells were assembled in an argon glovebox (O_2, H_2O < 1 ppm). The cells were rested for 3 h before measurements. In the LSV test, the cell voltage was scanned from the open circuit voltage to 6 V at a rate of 1 mV/s. In the potentiostatic hold test, the cell voltage was held for 3 h at each value from 3 to 6 V in 0.2 V intervals.

Li/Li Symmetric Cell Cycling. A Neware BTS4000 battery tester was used to cycle Li/Li coin cells with the following configuration: SS||Li||30 μL of electrolyte||1 Celgard separator||30 μL of electrolyte||Li. Celgard 2325 was used for most of the electrolytes except for 1 M $LiPF_6$ in EC/DMC (50:50 v/v), where Celgard 3501 was used for better wetting. Celgard 3501 separators were also cut into 18 mm diameter disks and dried at 70 °C overnight before use. The lithium electrode has a thickness of 750 μm and a diameter of 12 mm. All of the coin cells were assembled in an argon glovebox (O_2, H_2O < 1 ppm). After 10 h of resting and five formation cycles at 0.02 mA/cm^2 to 0.1 mA h/cm^2, the Li/Li cells were cycled at 1 mA/cm^2 to 1 mA h/cm^2. The cycling was performed at 20 °C, and the cutoff voltage was set to be 1 and −2 V.

The interfacial resistance measurements of Li/Li symmetric cells were done using EIS performed with a Biologic VSP-300 potentiostat from 7 MHz to 1 Hz at 20 °C. The impedance spectra were fitted by the circuit shown in Figure S26, and R2 was taken as interfacial resistance.

Coulombic Efficiency (CE) Measurement in Li/Cu Half Cells. A Neware BTS4000 battery tester was used to cycle Li/Cu coin cells with the following configuration: SS||Li||30 μL of electrolyte||1 Celgard separator||30 μL of electrolyte||Cu||SS. The lithium electrode has a thickness of 750 μm and a diameter of 12 mm, and the copper electrode has a diameter of 15 mm. All of the coin cells were assembled in an argon glovebox (O_2, H_2O < 1 ppm). In the CE test, cells were first precycled by depositing lithium on the copper electrode for 10 h and then stripping to 1 V. Then, a 10 h deposition was done. This was followed by 10, 2 h deposition and stripping cycles (yielding 1 mA h/cm^2). Finally, lithium was stripped from the copper electrode until the cell voltage reached 1 V. All of the deposition and stripping steps were performed at a current density of 0.5 mA/cm^2. CE was calculated as the ratio of total stripping capacity over total depositing capacity (except for the precycle).

Full Cell Cycling. The $LiFePO_4$ (LFP) electrode has a total mass loading of 13.40 mg/cm^2 with 90 wt % Johnson Matthey LFP, 5 wt % Timcal C-45, and 5 wt % Solvay 5130 PVDF binder. The $Li_4Ti_5O_{12}$ (LTO) electrode has a total mass loading of 14.10 mg/cm^2 with 87 wt % Samsung $Li_4Ti_5O_{12}$, 5 wt % Timcal C45, and 8 wt % Kureha 9300 PVDF binder. $LiNi_{1/3}Co_{1/3}Mn_{1/3}O_2$(NMC 111) electrode has a total mass loading of 11.22 mg/cm^2 with 90 wt % Toda NMC 111, 5 wt % Timcal C45, and 5 wt % Solvay 5130 PVDF binder. The electrodes were cut into 12 mm diameter disks and vacuum-dried at 120 °C overnight in a heated glovebox antechamber before use. The lithium electrode has a thickness of 750 μm and a diameter of 12 mm. All of the coin cells were assembled in an argon glovebox (O_2, H_2O < 1 ppm). Li/LFP coin cells were assembled in the following configuration: SS||Li||30 μL of electrolyte||1 Celgard separator||30 μL of electrolyte||LFP||SS. Celgard 2325 was used for most of the electrolytes except for 1 M $LiPF_6$ in EC/DMC (50:50 v/v), where Celgard 3501 was used for better wetting. Li/NMC 111 coin cells were assembled in the following configuration: SS||Li||30 μL of electrolyte||1 Celgard 2325 separator||30 μL of electrolyte||NMC 111||SS. LTO/NMC 111 coin cells were assembled in the following configuration: SS||LTO||30 μL of electrolyte||1 Celgard 2325 separator||30 μL of electrolyte||NMC 111||SS. The charging/discharging rate was calculated based on the exact mass of cathode material, using 150 mA h/g as the full capacity of LFP and 161 mA h/g as that of NMC 111. For an average mass loading of 12.1 mg LFP/cm^2, 1C ≈ 1.81 mA/cm^2. For an average mass loading of 10.1 mg NMC 111/cm^2,

https://doi.org/10.1021/acscentsci.1c00503
ACS Cent. Sci. 2021, 7, 1232−1244

1C ≈ 1.62 mA/cm^2. A Neware BTS4000 battery tester was used to cycle coin cells at 20 °C.

Simulations. *Density Functional Theory (DFT) Calculations.* DFT calculations were performed using the Gaussian 16 computational package.[44] All geometries were optimized at the B3LYP/6-31G(d,p) level of theory. After stationary points were verified by the absence of imaginary frequencies, single point energies of the optimized geometries were calculated using B3LYP/6-311++G(d,p). Solvent effects were accounted for by employing the SMD model.[45] THF was selected because of its moderate dielectric constant. Grimme's DFT-D3 method with BJ-damping (GD3BJ)[46] was used for dispersion correction. To calculate the adiabatic redox energy, the geometries of neutral and charged states were optimized, and their Gibbs free energies were calculated. The oxidation energy was defined as $G(M^+) - G(M)$ while the reduction energy was defined as $G(M) - G(M^-)$. The energies were divided by Faraday's constant, and then, 1.4 was subtracted from it to convert to electrochemical potentials (versus Li/Li$^+$).[47]

■ ASSOCIATED CONTENT

Supporting Information

The Supporting Information is available free of charge at https://pubs.acs.org/doi/10.1021/acscentsci.1c00503.

Additional data and figures including synthetic scheme, NMR spectra, FTIR spectra, GC-MS data, ionic conductivity data, activation energy values, DSC data, LSV data, DFT calculations, Raman spectra, SEM images, and battery cycling data (PDF)

■ AUTHOR INFORMATION

Corresponding Author

Chibueze V. Amanchukwu − *Pritzker School of Molecular Engineering, University of Chicago, Chicago, Illinois 60637, United States; Chemical Sciences and Engineering Division, Argonne National Laboratory, Lemont, Illinois 60439, United States;* orcid.org/0000-0002-6573-1213; Email: chibueze@uchicago.edu

Authors

Peiyuan Ma − *Pritzker School of Molecular Engineering, University of Chicago, Chicago, Illinois 60637, United States*

Priyadarshini Mirmira − *Pritzker School of Molecular Engineering, University of Chicago, Chicago, Illinois 60637, United States*

Complete contact information is available at: https://pubs.acs.org/10.1021/acscentsci.1c00503

Notes

The authors declare no competing financial interest.

■ ACKNOWLEDGMENTS

This work was supported by generous start-up funds from the University of Chicago. C.V.A. acknowledges V. Leboo for fruitful discussions. This work made use of the shared facilities (Raman, SEM) at the University of Chicago Materials Research Science and Engineering Center, supported by the National Science Foundation under Award DMR-2011854. Parts of this work (DSC, FTIR) were carried out at the Soft Matter Characterization Facility of the University of Chicago. NMR measurements were performed at the UChicago Chemistry NMR Facility. DFT calculations were performed with resources provided by the University of Chicago's Research Computing Center. The authors thank Steve Trask and Andrew Jansen at Argonne's Cell Analysis, Modeling, and Prototyping (CAMP) facility for providing the LTO, LFP, and NMC 111 electrodes.

■ REFERENCES

(1) Etacheri, V.; Marom, R.; Elazari, R.; Salitra, G.; Aurbach, D. Challenges in the Development of Advanced Li-Ion Batteries: A Review. *Energy Environ. Sci.* **2011**, *4*, 3243−3262.

(2) Goodenough, J. B.; Park, K.-S. The Li-Ion Rechargeable Battery: A Perspective. *J. Am. Chem. Soc.* **2013**, *135*, 1167.

(3) Lin, D.; Liu, Y.; Cui, Y. Reviving the Lithium Metal Anode for High-Energy Batteries. *Nat. Nanotechnol.* **2017**, *12*, 194−206.

(4) Liu, J.; Bao, Z.; Cui, Y.; Dufek, E. J.; Goodenough, J. B.; Khalifah, P.; Li, Q.; Yann Liaw, B.; Liu, P.; Manthiram, A.; Shirley Meng, Y.; Subramanian, V. R.; Toney, M. F.; Viswanathan, V. V.; Stanley Whittingham, M.; Xiao, J.; Xu, W.; Yang, J.; Yang, X.-Q.; Zhang, J.-G. Pathways for Practical High-Energy Long-Cycling Lithium Metal Batteries. *Nat. ENERGY* **2019**, *4*, 180.

(5) Gunnarsdóttir, A. B.; Amanchukwu, C. V.; Menkin, S.; Grey, C. P. Noninvasive In Situ NMR Study of "Dead Lithium" Formation and Lithium Corrosion in Full-Cell Lithium Metal Batteries. *J. Am. Chem. Soc.* **2020**, *142*, 20814−20827.

(6) Wood, K. N.; Kazyak, E.; Chadwick, A. F.; Chen, K.-H.; Zhang, J.-G.; Thornton, K.; Dasgupta, N. P. Dendrites and Pits: Untangling the Complex Behavior of Lithium Metal Anodes through Operando Video Microscopy. *ACS Cent. Sci.* **2016**, *2*, 790.

(7) Xu, K. Electrolytes and Interphases in Li-Ion Batteries and Beyond. *Chem. Rev.* **2014**, *114* (23), 11503−11618.

(8) Winter, M.; Barnett, B.; Xu, K. Before Li Ion Batteries. *Chem. Rev.* **2018**, *118* (23), 11433−11456.

(9) Xu, K. Nonaqueous Liquid Electrolytes for Lithium-Based Rechargeable Batteries. *Chem. Rev.* **2004**, *104* (10), 4303−4418.

(10) Ding, F.; Xu, W.; Chen, X.; Zhang, J.; Engelhard, M. H.; Zhang, Y.; Johnson, B. R.; Crum, J. V.; Blake, T. A.; Liu, X.; Zhang, J.-G. Effects of Carbonate Solvents and Lithium Salts on Morphology and Coulombic Efficiency of Lithium Electrode. *J. Electrochem. Soc.* **2013**, *160* (10), A1894−A1901.

(11) Chen, S.; Zheng, J.; Mei, D.; Han, K. S.; Engelhard, M. H.; Zhao, W.; Xu, W.; Liu, J.; Zhang, J.-G. High-Voltage Lithium-Metal Batteries Enabled by Localized High-Concentration Electrolytes. *Adv. Mater.* **2018**, *30* (21), 1706102.

(12) Qian, J.; Henderson, W. A.; Xu, W.; Bhattacharya, P.; Engelhard, M.; Borodin, O.; Zhang, J.-G. High Rate and Stable Cycling of Lithium Metal Anode. *Nat. Commun.* **2015**, *6* (1), 6362.

(13) Jiao, S.; Ren, X.; Cao, R.; Engelhard, M. H.; Liu, Y.; Hu, D.; Mei, D.; Zheng, J.; Zhao, W.; Li, Q.; Liu, N.; Adams, B. D.; Ma, C.; Liu, J.; Zhang, J.-G.; Xu, W. Stable Cycling of High-Voltage Lithium Metal Batteries in Ether Electrolytes. *Nat. Energy* **2018**, *3*, 739−746.

(14) Amanchukwu, C. V.; Kong, X.; Qin, J.; Cui, Y.; Bao, Z. Nonpolar Alkanes Modify Lithium-Ion Solvation for Improved Lithium Deposition and Stripping. *Adv. Energy Mater.* **2019**, *9* (41), 1902116.

(15) Yu, Z.; Wang, H.; Kong, X.; Huang, W.; Tsao, Y.; Mackanic, D. G.; Wang, K.; Wang, X.; Huang, W.; Choudhury, S.; Zheng, Y.; Amanchukwu, C. V.; Hung, S. T.; Ma, Y.; Lomeli, E. G.; Qin, J.; Cui, Y.; Bao, Z. Molecular Design for Electrolyte Solvents Enabling Energy-Dense and Long-Cycling Lithium Metal Batteries. *Nat. Energy* **2020**, *5*, 526−533.

(16) Harding, J. R.; Amanchukwu, C. V.; Hammond, P. T.; Shao-Horn, Y. Instability of Poly(Ethylene Oxide) upon Oxidation in Lithium-Air Batteries. *J. Phys. Chem. C* **2015**, *119* (13), 6947−6955.

(17) Amanchukwu, C. V. The Electrolyte Frontier: A Manifesto. *Joule* **2020**, *4* (2), 281−285.

(18) Yamada, Y.; Yamada, A. Review—Superconcentrated Electrolytes for Lithium Batteries. *J. Electrochem. Soc.* **2015**, *162* (14), A2406−A2423.

(19) Yamada, Y.; Furukawa, K.; Sodeyama, K.; Kikuchi, K.; Yaegashi, M.; Tateyama, Y.; Yamada, A. Unusual Stability of Acetonitrile-Based Superconcentrated Electrolytes for Fast-Charging Lithium-Ion Batteries. *J. Am. Chem. Soc.* **2014**, *136* (13), 5039−5046.
(20) Yoshida, K.; Nakamura, M.; Kazue, Y.; Tachikawa, N.; Tsuzuki, S.; Seki, S.; Dokko, K.; Watanabe, M. Oxidative-Stability Enhancement and Charge Transport Mechanism in GlymeÀLithium Salt Equimolar Complexes. *J. Am. Chem. Soc.* **2011**, *133*, 13121−13129.
(21) Qian, J.; Henderson, W. A.; Xu, W.; Bhattacharya, P.; Engelhard, M.; Borodin, O.; Zhang, J.-G. High Rate and Stable Cycling of Lithium Metal Anode. *Nat. Commun.* **2015**, *6* (1), 6362.
(22) Yamada, Y.; Wang, J.; Ko, S.; Watanabe, E.; Yamada, A. Advances and Issues in Developing Salt-Concentrated Battery Electrolytes. *Nat. Energy* **2019**, *4*, 269−280.
(23) Cao, X.; Ren, X.; Zou, L.; Engelhard, M. H.; Huang, W.; Wang, H.; Matthews, B. E.; Lee, H.; Niu, C.; Arey, B. W.; Cui, Y.; Wang, C.; Xiao, J.; Liu, J.; Xu, W.; Zhang, J.-G. Monolithic Solid-Electrolyte Interphases Formed in Fluorinated Orthoformate-Based Electrolytes Minimize Li Depletion and Pulverization. *Nat. Energy.* **2019**, *4*, 796.
(24) Perez Beltran, S.; Cao, X.; Zhang, J.-G.; Balbuena, P. B. Localized High Concentration Electrolytes for High Voltage Lithium-Metal Batteries: Correlation between the Electrolyte Composition and Its Reductive/Oxidative Stability. *Chem. Mater.* **2020**, *32*, 5973.
(25) Zhang, Z.; Hu, L.; Wu, H.; Weng, W.; Koh, M.; Redfern, P. C.; Curtiss, L. A.; Amine, K. Fluorinated Electrolytes for 5 V Lithium-Ion Battery Chemistry. *Energy Environ. Sci.* **2013**, *6* (6), 1806−1810.
(26) Amanchukwu, C. V.; Yu, Z.; Kong, X.; Qin, J.; Cui, Y.; Bao, Z. A New Class of Ionically Conducting Fluorinated Ether Electrolytes with High Electrochemical Stability. *J. Am. Chem. Soc.* **2020**, *142* (16), 7393−7403.
(27) Xue, W.; Huang, M.; Li, Y.; Guang Zhu, Y.; Gao, R.; Xiao, X.; Zhang, W.; Li, S.; Xu, G.; Yu, Y.; Li, P.; Lopez, J.; Yu, D.; Dong, Y.; Fan, W.; Shi, Z.; Xiong, R.; Sun, C.-J.; Hwang, I.; Lee, W.-K.; Shao-Horn, Y.; Johnson, J. A.; Li, J. Ultra-High-Voltage Ni-Rich Layered Cathodes in Practical Li Metal Batteries Enabled by a Sulfonamide-Based Electrolyte. *Nat. Energy* **2021**, *6*, 495.
(28) Feng, S.; Huang, M.; Lamb, J. R.; Perkinson, C. F.; Johnson, J. A.; Shao-Horn, Y.; Zhang, W.; Tatara, R.; Zhang, Y.; Zhu, Y. G. Molecular Design of Stable Sulfamide-and Sulfonamide-Based Electrolytes for Aprotic Li-O 2 Batteries. *CHEMPR* **2019**, *5*, 2630.
(29) Horowitz, Y.; Han, H.-L.; Ralston, W. T.; de Araujo, J. R.; Kreidler, E.; Brooks, C.; Somorjai, G. A. Fluorinated End-Groups in Electrolytes Induce Ordered Electrolyte/Anode Interface Even at Open-Circuit Potential as Revealed by Sum Frequency Generation Vibrational Spectroscopy. *Adv. Energy Mater.* **2017**, *7* (17), 1602060.
(30) Wang, J.; Yamada, Y.; Sodeyama, K.; Chiang, C. H.; Tateyama, Y.; Yamada, A. Superconcentrated Electrolytes for a High-Voltage Lithium-Ion Battery. *Nat. Commun.* **2016**, *7* (1), 12032.
(31) Chen, S.; Yu, Z.; Gordin, M. L.; Yi, R.; Song, J.; Wang, D. A Fluorinated Ether Electrolyte Enabled High Performance Prelithiated Graphite/Sulfur Batteries. *ACS Appl. Mater. Interfaces* **2017**, *9* (8), 6959−6966.
(32) Huang, M.; Feng, S.; Zhang, W.; Giordano, L.; Chen, M.; Amanchukwu, C. V.; Anandakathir, R.; Shao-Horn, Y.; Johnson, J. A. Fluorinated Aryl Sulfonimide Tagged (FAST) Salts: Modular Synthesis and Structure-Property Relationships for Battery Applications. *Energy Environ. Sci.* **2018**, *11* (5), 1326−1334.
(33) Feng, S.; Chen, M.; Giordano, L.; Huang, M.; Zhang, W.; Amanchukwu, C. V.; Anandakathir, R.; Shao-Horn, Y.; Johnson, J. A. Mapping a Stable Solvent Structure Landscape for Aprotic Li-Air Battery Organic Electrolytes. *J. Mater. Chem. A* **2017**, *5* (45), 23987−23998.
(34) Brouillette, D.; Irish, D. E.; Taylor, N. J.; Perron, G.; Odziemkowski, M.; Desnoyers, J. E. Stable Solvates in Solution of Lithium Bis(Trifluoromethylsulfone)Imide in Glymes and Other Aprotic Solvents: Phase Diagrams, Crystallography and Raman Spectroscopy. *Phys. Chem. Chem. Phys.* **2002**, *4* (24), 6063−6071.
(35) Lukatskaya, M. R.; Feldblyum, J. I.; Mackanic, D. G.; Lissel, F.; Michels, D. L.; Cui, Y.; Bao, Z. Concentrated Mixed Cation Acetate "Water-in-Salt" Solutions as Green and Low-Cost High Voltage Electrolytes for Aqueous Batteries. *Energy Environ. Sci.* **2018**, *11* (10), 2876−2883.
(36) Qiao, B.; Leverick, G. M.; Zhao, W.; Flood, A. H.; Johnson, J. A.; Shao-Horn, Y. Supramolecular Regulation of Anions Enhances Conductivity and Transference Number of Lithium in Liquid Electrolytes. *J. Am. Chem. Soc.* **2018**, *140* (35), 10932−10936.
(37) Holoubek, J.; Liu, H.; Wu, Z.; Yin, Y.; Xing, X.; Cai, G.; Yu, S.; Zhou, H.; Pascal, T. A.; Chen, Z.; Liu, P. Tailoring Electrolyte Solvation for Li Metal Batteries Cycled at Ultra-Low Temperature. *Nat. Energy* **2021**, *6*, 303.
(38) Adams, B. D.; Zheng, J.; Ren, X.; Xu, W.; Zhang, J.-G. Accurate Determination of Coulombic Efficiency for Lithium Metal Anodes and Lithium Metal Batteries. *Adv. Energy Mater.* **2018**, *8* (7), 1702097.
(39) Homann, G.; Stolz, L.; Nair, J.; Laskovic, I. C.; Winter, M.; Kasnatscheew, J. Poly(Ethylene Oxide)-Based Electrolyte for Solid-State-Lithium-Batteries with High Voltage Positive Electrodes: Evaluating the Role of Electrolyte Oxidation in Rapid Cell Failure. *Sci. Rep.* **2020**, *10* (1), 4390.
(40) Boyle, D. T.; Huang, W.; Wang, H.; Li, Y.; Chen, H.; Yu, Z.; Zhang, W.; Bao, Z.; Cui, Y. Corrosion of Lithium Metal Anodes during Calendar Ageing and Its Microscopic Origins. *Nat. Energy* **2021**, *6* (5), 487−494.
(41) Krajewski, M.; Hamankiewicz, B.; Michalska, M.; Andrzejczuk, M.; Lipinska, L.; Czerwinski, A. Electrochemical Properties of Lithium-Titanium Oxide, Modified with Ag-Cu Particles, as a Negative Electrode for Lithium-Ion Batteries. *RSC Adv.* **2017**, *7* (82), 52151−52164.
(42) Günther, H. Lithium NMR. In *eMagRes*; John Wiley & Sons, 2007. DOI: 10.1002/9780470034590.emrstm0273.
(43) Li, C.; Suzuki, K.; Yamaguchi, K.; Mizuno, N. Phosphovanadomolybdic Acid Catalyzed Direct C-H Trifluoromethylation of (Hetero)Arenes Using NaSO2CF3 as the CF3 Source and O2 as the Terminal Oxidant. *New J. Chem.* **2017**, *41* (4), 1417−1420.
(44) Frisch, M. J.; Trucks, G. W.; Schlegel, H. B.; Scuseria, G. E.; Robb, M. A.; Cheeseman, J. R.; Scalmani, G.; Barone, V.; Petersson, G. A.; Nakatsuji, H.; Li, X.; Caricato, M.; Marenich, A. V.; Bloino, J.; Janesko, B. G.; Gomperts, R.; Mennucci, B.; Hratchian, H. P.; Ortiz, J. V.; Izmaylov, A. F.; Sonnenberg, J. L.; Williams-Young, D.; Ding, F.; Lipparini, F.; Egidi, F.; Goings, J.; Peng, B.; Petrone, A.; Henderson, T.; Ranasinghe, D.; Zakrzewski, V. G.; Gao, J.; Rega, N.; Zheng, G.; Liang, W.; Hada, M.; Ehara, M.; Toyota, K.; Fukuda, R.; Hasegawa, J.; Ishida, M.; Nakajima, T.; Honda, Y.; Kitao, O.; Nakai, H.; Vreven, T.; Throssell, K.; Montgomery, J. A., Jr.; Peralta, J. E.; Ogliaro, F.; Bearpark, M.; Heyd, J. J.; Brothers, E. N.; Kudin, K. N.; Staroverov, V. N.; Kobayashi, R.; Normand, J.; Raghavachari, K.; Rendell, A.; Burant, J. C.; Iyengar, S. S.; Tomasi, J.; Cossi, M.; Millam, J. M.; Klene, M.; Adamo, C.; Cammi, R.; Ochterski, J. W.; Martin, R. L.; Morokuma, K.; Farkas, O.; Foresman, J. B.; Fox, D. J. *Gaussian 16*, revision A.03; Gaussian, Inc.: Wallingford CT, 2016.
(45) Marenich, A. V.; Cramer, C. J.; Truhlar, D. G. Universal Solvation Model Based on Solute Electron Density and on a Continuum Model of the Solvent Defined by the Bulk Dielectric Constant and Atomic Surface Tensions. *J. Phys. Chem. B* **2009**, *113* (18), 6378−6396.
(46) Grimme, S.; Ehrlich, S.; Goerigk, L. Effect of the Damping Function in Dispersion Corrected Density Functional Theory. *J. Comput. Chem.* **2011**, *32* (7), 1456−1465.
(47) Borodin, O.; Behl, W.; Jow, T. R. Oxidative Stability and Initial Decomposition Reactions of Carbonate, Sulfone, and Alkyl Phosphate-Based Electrolytes. *J. Phys. Chem. C* **2013**, *117* (17), 8661−8682.

https://doi.org/10.1021/acscentsci.1c00503
ACS Cent. Sci. 2021, 7, 1232−1244